Clim Dyn (2016) 47:2039–2057
DOI 10.1007/s00382-015-2949-7

Coupled intraseasonal variations in the East Asian winter monsoon and the South China Sea–western North Pacific SST in boreal winter

Renguang Wu[1]

Received: 9 June 2015 / Accepted: 10 December 2015 / Published online: 17 December 2015

Abstract The sea surface temperature (SST) in the South China Sea (SCS) displays prominent intraseasonal variations during boreal winter with a spectrum peak in the 10–30-day time period. These intraseasonal SST variations are closely associated with intraseasonal variations of the East Asian winter monsoon (EAWM). A weak EAWM is preceded by cooler SST and followed by warmer SST in the SCS and subtropical western North Pacific. A coherent southward propagation is seen in the SCS in SST, surface wind, and latent heat flux anomalies. This southward propagation is attributed to the wind-evaporation-SST effect under climatological northerly winds in winter, which differs from summer when climatological winds are westerly. The SST-induced wind speed anomalies are larger to the north side of SST anomalies. This induces larger surface evaporation anomalies to the north side, leading to a southward displacement of large SST anomalies. In turn, wind and evaporation anomalies move southward. There appears to be a positive feedback between circulation and precipitation that leads to amplification of meridional wind anomalies when the SST anomalies are weak. Surface latent heat flux is a dominant factor for the SST change in the SCS and the Yellow Sea. Shortwave radiation has a complementary contribution to the SST change in the SCS, but has a negative effect in the Yellow Sea. The wind-induced Ekman advection appears important for the SST warming in the Yellow Sea.

Keywords East Asian winter monsoon · South China Sea SST · Coupled intraseasonal variation · Southward propagation · Boreal winter

1 Introduction

The intraseasonal oscillation (ISO) is an important component of climate variability over the tropical Indo-western Pacific region. It is closely related to the active and break phases of the summer monsoon. There is indication for a coupled intraseasonal variation in sea surface temperature (SST) and atmospheric ISO in the tropical Indo-western Pacific region (e.g., Waliser et al. 1999, 2004; Woolnough et al. 2000; Maloney and Sobel 2004; Duvel and Vialard 2007; Ye and Wu 2015), which may affect the characteristics and propagations of atmospheric ISOs (e.g., Kemball-Cook and Wang 2001; Fu et al. 2003; Wu 2010; Roxy and Tanimoto 2007, 2011; Roxy et al. 2013). Thus, it is important to understand the coupled processes between variations of SST and atmospheric variables on intraseasonal time scales and their impacts for the purpose of improving the understanding and prediction of intraseasonal variability.

While studies have been conducted about the atmosphere–ocean coupling in intraseasonal variations in the South China Sea (SCS) and western North Pacific region (Xie et al. 2007; Wu et al. 2008; Wu 2010; Roxy and Tanimoto 2011; Ye and Wu 2015), most previous studies are concerned with intraseasonal variations during boreal summer. Little has been done about intraseasonal variations in the SCS and western North Pacific region during boreal winter. This appears to relate to the fact that convection

---

✉ Renguang Wu
Renguang@mail.iap.ac.cn

[1] Center for Monsoon System Research and State Key Laboratory of Numerical Modeling for Atmospheric Sciences and Geophysical Fluid Dynamics, Institute of Atmospheric Physics, Chinese Academy of Sciences, Building 40, Huayanli, Beichen West Road, Chaoyang District, Beijing 100029, China

is weak over the Northern Hemisphere in boreal winter. Nevertheless, due to the influence of the East Asian winter monsoon (EAWM) variability, large wind variability may occur in winter over the SCS region. As the wind changes may affect surface evaporation, oceanic upwelling and advection, large SST fluctuations may be induced by EAWM-related wind changes (Wu and Chen 2015). Zeng and Wang (2009) obtained larger intraseasonal variance of latent heat flux over the South China Sea in winter than in summer. Based on analysis of pentad mean data, Gao and Zhou (2002) noted that the 30–90 day intraseasonal SST variations in the South China Sea display different characteristics in winter from those in summer. In summer, the intraseasonal SST perturbations feature a zonal distribution, a northeastward propagation, and a close relation to zonal wind and convection variations. In contrast, they appear to be localized in the SCS region without any propagating signal and are primarily associated with meridional wind variations in winter. Yet, it is not clear how intraseasonal SST and wind variations in winter are coupled to each other over the SCS and western North Pacific region. One purpose of the present study is to investigate the coupled SST and wind variations associated with the EAWM on the intraseasonal time scales in the above region.

In boreal summer, the ISOs display northward or northeastward propagation over the Indian summer monsoon region (Yasunari 1979; Jiang et al. 2004; Chou and Hsueh 2010) and northward or northwestward propagation over the western North Pacific region (Wang and Wu 1997; Annamalai and Slingo 2001; Hsu and Weng 2001; Kemball-Cook and Wang 2001; Kajikawa and Yasunari 2005) in conjunction with the eastward propagation along the equator. In boreal winter, the prevailing direction of propagation of ISOs is eastward along the equator, accompanied by poleward propagation over off-equatorial regions of tropical Indo-western Pacific Ocean (Wheeler and Kiladis 1999; Lawrence and Webster 2002; Zhang 2005; Wang et al. 2006).

Our analysis detects a southward propagation in intraseasonal signals of both SST and meridional wind over the SCS and subtropical western North Pacific in boreal winter. Figure 1 displays diagrams of SST and 10 m merional wind variations on the 9–31-day time period along 110°–120°E during November through March for years 2002/2003, 2003/2004, 2005/2006, and 2007/2008. These 4 years are selected for purpose of illustration. Southward propagation of meridional wind anomalies is a robust phenomenon over the subtropics. Prominent southward propagation to the tropics can be observed in both SST and meridional wind anomalies in some periods, for example, during mid-December of 2002 through late January of 2003, during late February through early March of 2003, during early January through early March of 2004, during mid-November through mid-December of 2005, around mid-January of 2006, and during early to mid-January of 2008. During these periods, southerly or northerly wind anomalies appear first over southern China and move southward to central and southern SCS. These are followed by southward propagation of positive or negative SST anomalies from northern to central or southern SCS. The phase relationship appears to suggest a coupled intraseasonal propagation in SST and surface wind anomalies. Thus, another purpose of the present study is to understand this unique southward propagation and the relevant processes.

The southward propagation of SST anomalies in the SCS was pointed out by Wu and Chen (2015) on the 7–61-day time scale. Different from Wu and Chen (2015), this study focuses on the 9–31-day time scale on which SCS SST and EAWM display common spectral peak, as will be shown later. Wu and Chen (2015) documented the feature of southward propagation of different variables in the SCS region, but did not address whether and how they are coupled with each other. Distinct from Wu and Chen (2015), the present study address the coupled processes in the southward propagation of SST, surface wind, and surface heat fluxes. Another different from Wu and Chen (2015) is that the present study extends the region of analysis to the western North Pacific.

The organization of the text is as follows. Section 2 describes the datasets and methods used in the present study. Section 3 provides evidence for intraseasonal signals in SCS SST and EAWM variations. The spatial–temporal evolution of intraseasonal anomalies associated with the EAWM is presented in Sect. 4. Section 5 analyzes the connection of southward propagation in different variables to understand the physical processes. Summary and discussions are given in Sect. 6.

2 Datasets and methods

Present study uses daily SST, rain rate, cloud liquid water (CLD), surface wind speed at 37 GHz from the Tropical Rainfall Measuring Mission (TRMM) Microwave Imager (TMI) (Wentz et al. 2000) for the period 1998–2013. The TMI data are available on 0.25° × 0.25° grids. We have converted the original data to 1° × 1° grids to reduce the missing data. Further, 3-day running mean is used in the present study. The TMI data are obtained from http://www.remss.com/missions/tmi. The Global Precipitation Climatology Project (GPCP) version 2 (Adler et al. 2003) daily precipitation on 1° × 1° grids for the period October 1996—present is used to get information of precipitation variations over land where TMI is unavailable. The GPCP precipitation is obtained from https://climatedataguide.ucar.edu/climate-data/gpcp-daily-global-precipitation-climatology-project.

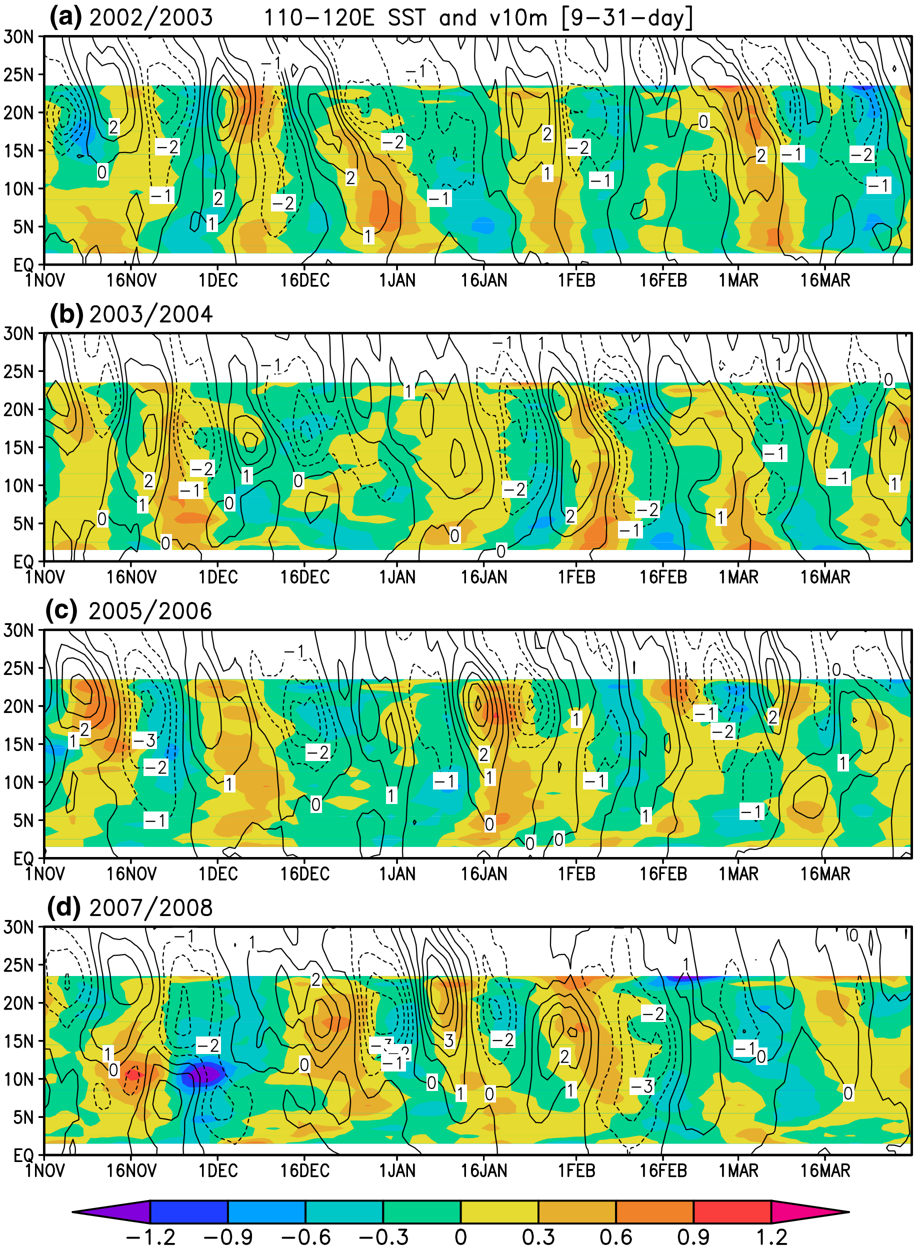

Fig. 1 Hovmöller diagrams of SST (*shading*, unit: °C) and 10 m meridional wind (contour, interval: 1 m/s) anomalies at the 9–31-day band along 110°–120°E during November 1 through March 31 of **a** 2002/2003, **b** 2003/2004, **c** 2005/2006, and **d** 2007/2008

We use daily surface winds at 10 m, surface latent heat flux (LHF), surface sensible heat flux (SHF), surface net shortwave radiation (SWR), and surface net longwave radiation (LWR) from the National Centers for Environmental Prediction (NCEP)-Department of Energy reanalysis 2 (Kanamitsu et al. 2002) for the period 1979–2013. These reanalysis variables are available on T62 Gaussian grids. The reanalysis data are obtained from ftp://cdc.noaa.gov/. The convention for surface heat flux is positive for downward shortwave radiation, but for upward longwave radiation, latent and sensible heat flux.

As this study is concerned with intraseasonal variations in the tropical and subtropical regions associated with the EAWM, we use an EAWM index (EAWMI) defined using area-mean meridional wind at 10 m averaged over the region of 10°–25°N, 105°–135°E. According to Chen et al. (2014), the above index represents the southern component of the EAWM variability. A positive (negative) EAWMI denotes a weak (strong) EAWM under this definition. Area-mean SCS SST in this study refers to SST averaged in the region of 5°–20°N, 105°–120°E.

Intraseasonal variations in this study refer to the component on the 9–31-day time period. The reason for focusing on this component will be illustrated later. We use 9-day running mean minus 31-day running mean to obtain the intraseasonal variations on the above time period. Use of

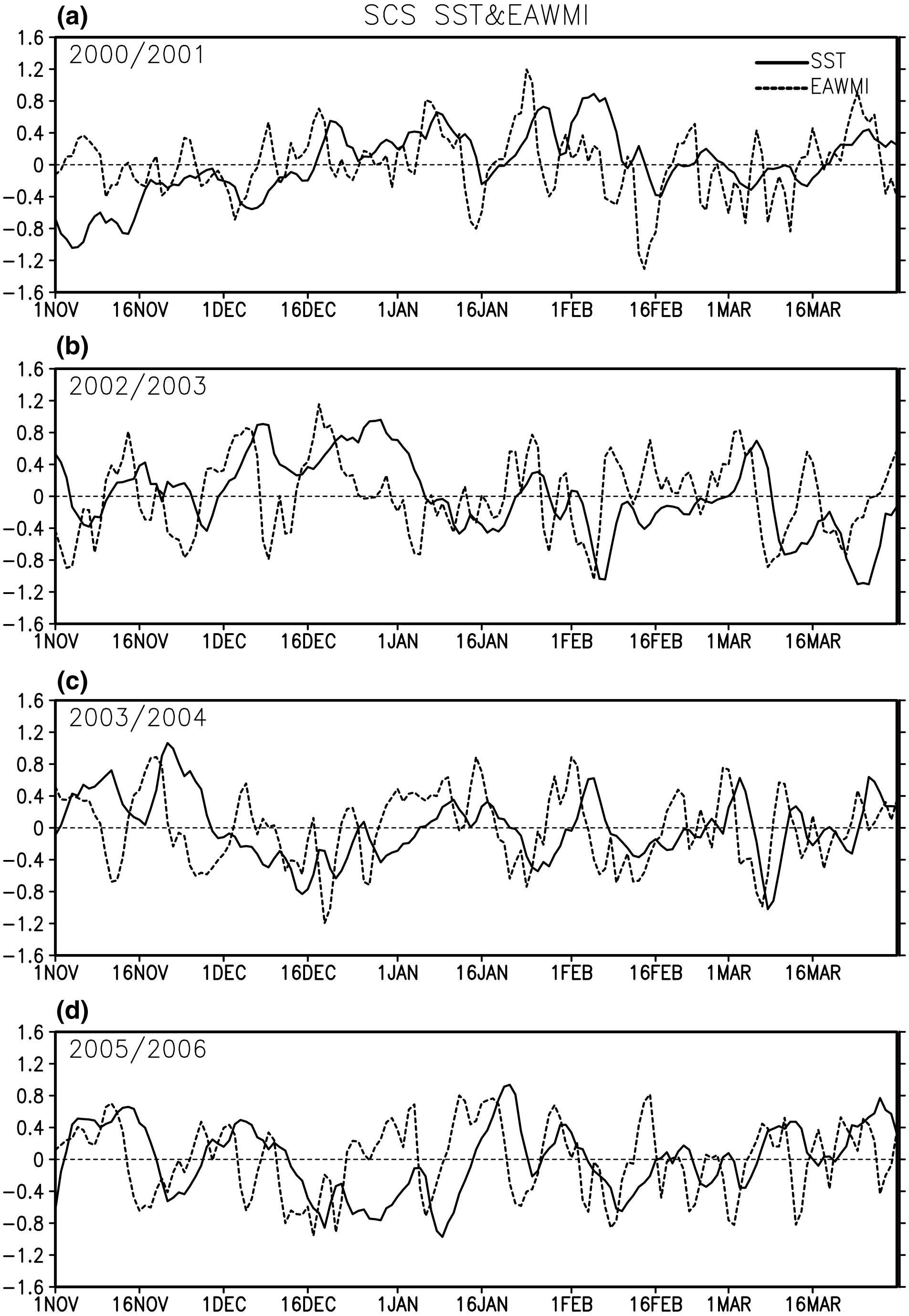

Fig. 2 Time series of SCS SST anomalies (*solid lines* with scale at left, unit: °C) and EAWMI (*dashed lines* with sale at right, unit: m/s) during November 1 through March 31 of **a** 2002/2003, **b** 2003/2004, **c** 2005/2006, and **d** 2007/2008

a band pass filter on the same time period leads to similar results but with smoother temporal evolution. Present study focuses on boreal winter, that is, December to February (DJF), which is the peak EAWM season. The analysis period is from 1998/1999 to 2012/2013 when all the variables are available.

3 Signals of intraseasonal variations in EAWM and SCS SST

The EAWMI and SCS SST display notable intraseasonal variations during boreal winter. Figure 2 shows EAWMI and SCS SST anomalies during November through March

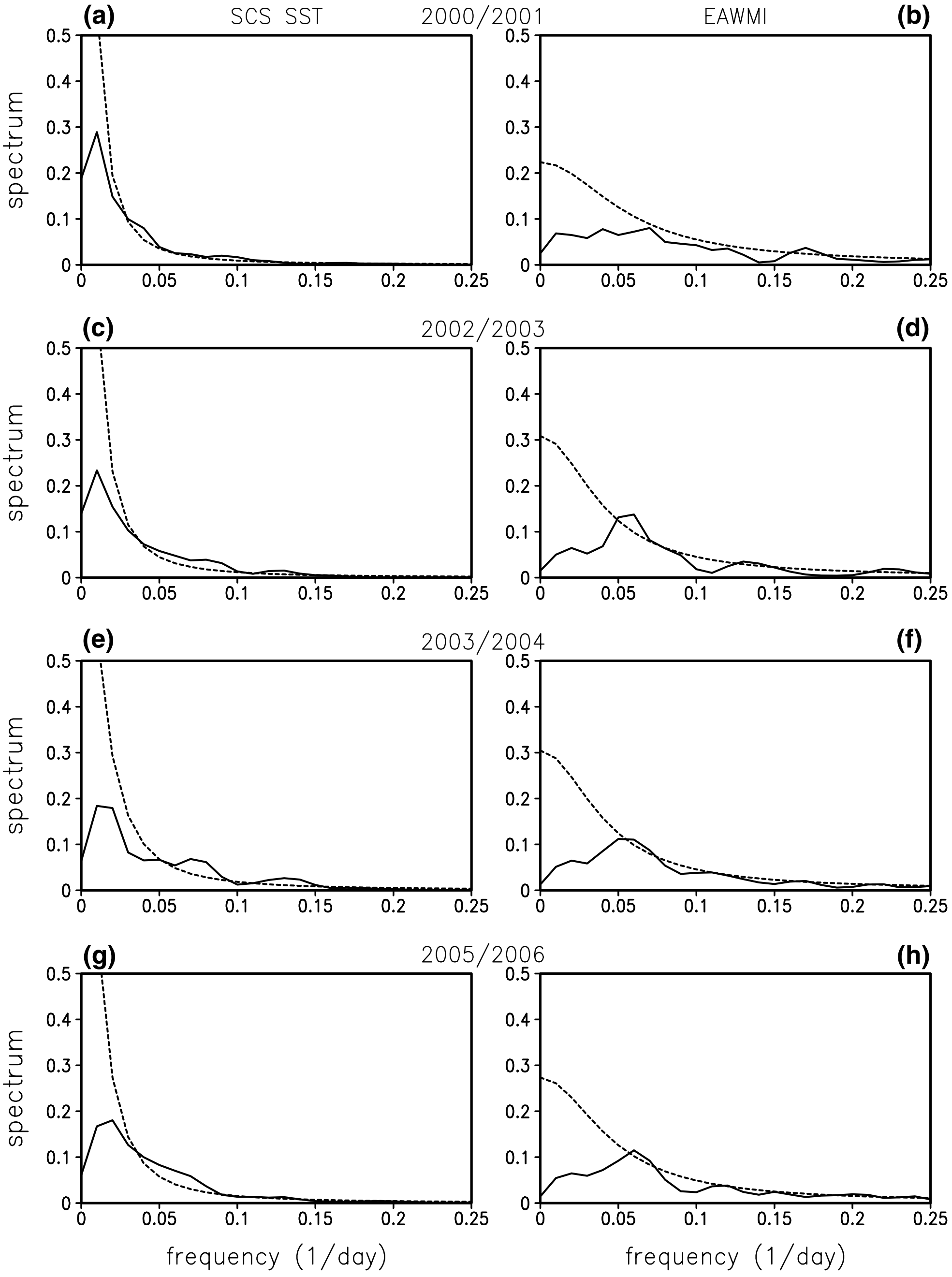

Fig. 3 Spectrum of SCS SST (*left*) and EAWMI (*right*) for the period December 1 through February 28 of **a**, **b** 2000/2001, **c**, **d** 2002/2003, **e**, **f** 2003/2004, and **g**, **h** 2005/2006. *Dashed lines* denote the 95 % confidence level based on red noise spectrum

for years (a) 2002/2003, (b) 2003/2004, (c) 2005/2006, and (d) 2007/2008 for purpose of illustration. Obviously, there are alternative peaks and valleys in both EAWMI and SCS SST variations. The magnitude of area-mean SST anomalies reaches 1 °C in some cases and that of the EAWMI reaches 5 m/s or more, indicating a large intraseasonal signal. The time interval between peaks (valleys) varies from case to case, but with a dominant interval of about 10 days to 1 month between major peaks (valleys). Another feature to note on Fig. 2 is that there is a temporal phase shift between the SCS SST and EAWMI intraseasonal variations. EAWMI peaks tend to lead SCS SST peaks and EAWMI valleys tend to occur before SCS SST valleys. This phase relation signifies a coupled intraseasonal variation between the SCS SST and EAWM. This will be elaborated later.

The intraseasonal variations in EAWMI and SCS SST are confirmed by their spectrum. Figure 3 displays the

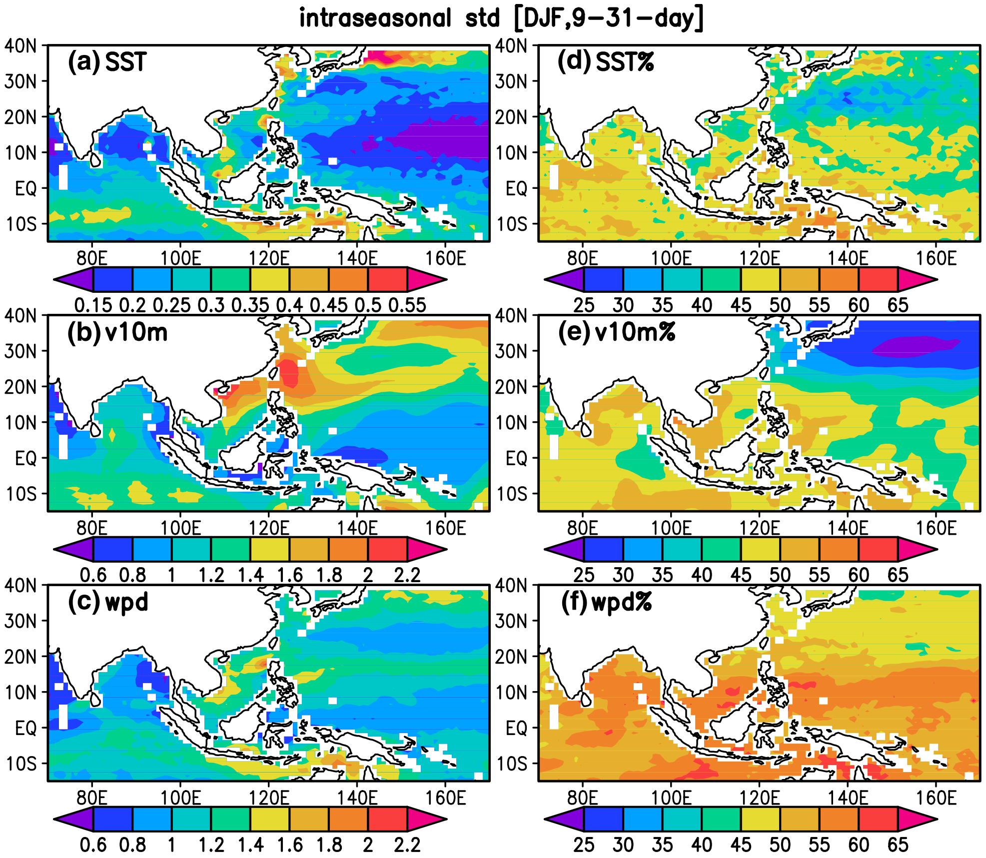

Fig. 4 Standard deviation of anomalies of SST (°C) (**a**), 10 m meridional wind (m/s) (**b**), and surface wind speed (m/s) (**c**) on 9-31-day time scale and the explained percent variance of total intraseasonal variance (**d**–**f**) during December through February

spectrum of the SCS SST and EAWMI during November through March for the years 2000/2001, 2002/2003, 2003/2004, and 2005/2006. The SCS SST spectrum displays a peak in the 10–30-day band and another peak with period longer than 40 days. The former peak is significant at the 95 % confidence level based on the red noise spectrum. The latter peak is insignificant likely due to the short time period. The EAWMI spectrum shows a prominent peak in the 10–30-day band as well. The peak with periods longer than 40 days is visible but much weaker compared to SST. There are peaks with periods shorter than 10 days, suggestive of synoptic activity. The present study focuses on the intraseasonal variations on the 10–30-day time scale on which both SCS SST and EAWMI display prominent spectrum peaks, which differs from Wu and Chen (2015) that analyzed the intraseasonal variations on the broad 7–61-day band.

The SST and surface wind variations on the 9–31-day time scale account for about 40–60 % of the total intraseasonal variations in the SCS region during boreal winter. Figure 4 shows the standard deviation of SST, 10 m meridional wind, and surface wind speed anomalies on the 9–31-day band and the explained percent variance with respect to the total intraseasonal variations for December through February. The SCS displays a relatively large 9–31-day variability in SST and surface wind speed (Fig. 4a, c). Larger standard deviation of meridional wind is seen over northern SCS and subtropical western North Pacific (Fig. 4b), likely related to large mean winds in these regions during winter. The percent variance accounted for by variations in the 9–31-day band in the SCS region is about 40–50 % for SST (Fig. 4d), 45–55 % for 10 m meridional wind (Fig. 4e), and 50–60 % for surface wind speed (Fig. 4f), respectively.

The time lag relation between intraseasonal variations of SCS SST and EAWMI is further demonstrated by a lag-lead correlation analysis. Figure 5 shows the correlation of SCS SST with respect to EAWMI on the 9–31-day time scale calculated for the period of December through February for the 4 years. Clearly, high SST appears at a few days after the peak EAWMI and low SST is seen about 1 week before the EAWMI peak. This suggests a coupled intraseasonal variation between SCS SST and EAWM. The time lead or lag of maximum correlation varies from year to year, so is the magnitude of the maximum lead or lag correlation. This suggests a year-to-year change in the coupling strength and the phase relation. Nevertheless, the coupled

Fig. 5 Lead-lag correlation of SCS SST anomalies with respect to EAWMI at the 9–31-day band during December 1 through February 28 of **a** 2000/2001, **b** 2002/2003, **c** 2003/2004, and **d** 2005/2006

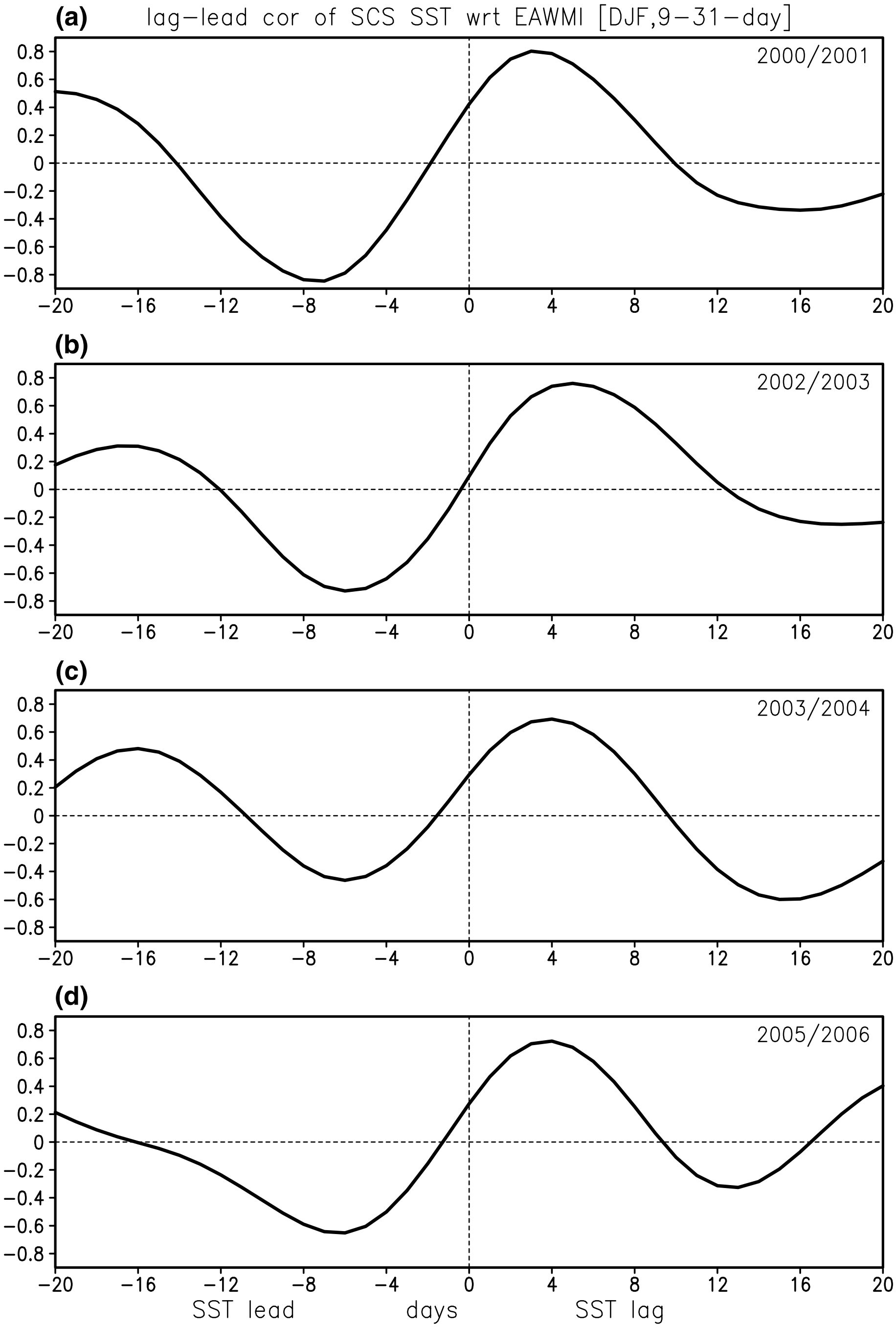

variability is robust. The specific processes of coupling the intraseasonal variations of SST and EAWM will be investigated in the next two sections.

4 Spatial–temporal evolution of intraseasonal anomalies associated with EAWM

To understand the coupled variations, we examine the spatial–temporal evolution of intraseasonal anomalies of SST, rain, surface wind, and surface heat fluxes on the 9–31-day time period. We take the normalized EAWMI as a reference to construct the anomalies through lag-lead regression. The results are shown in Fig. 6 for SST, rain, and 10 m winds, in Fig. 8 for surface wind speed and latent heat flux, and in Fig. 9 for cloud liquid water and surface net shortwave radiation for DJF. The anomalies shown in these figures start from 8 days before (lead −8) to 6 days after (lead +6) the peak EAWMI. Lead 0 denotes the time of peak EAWMI.

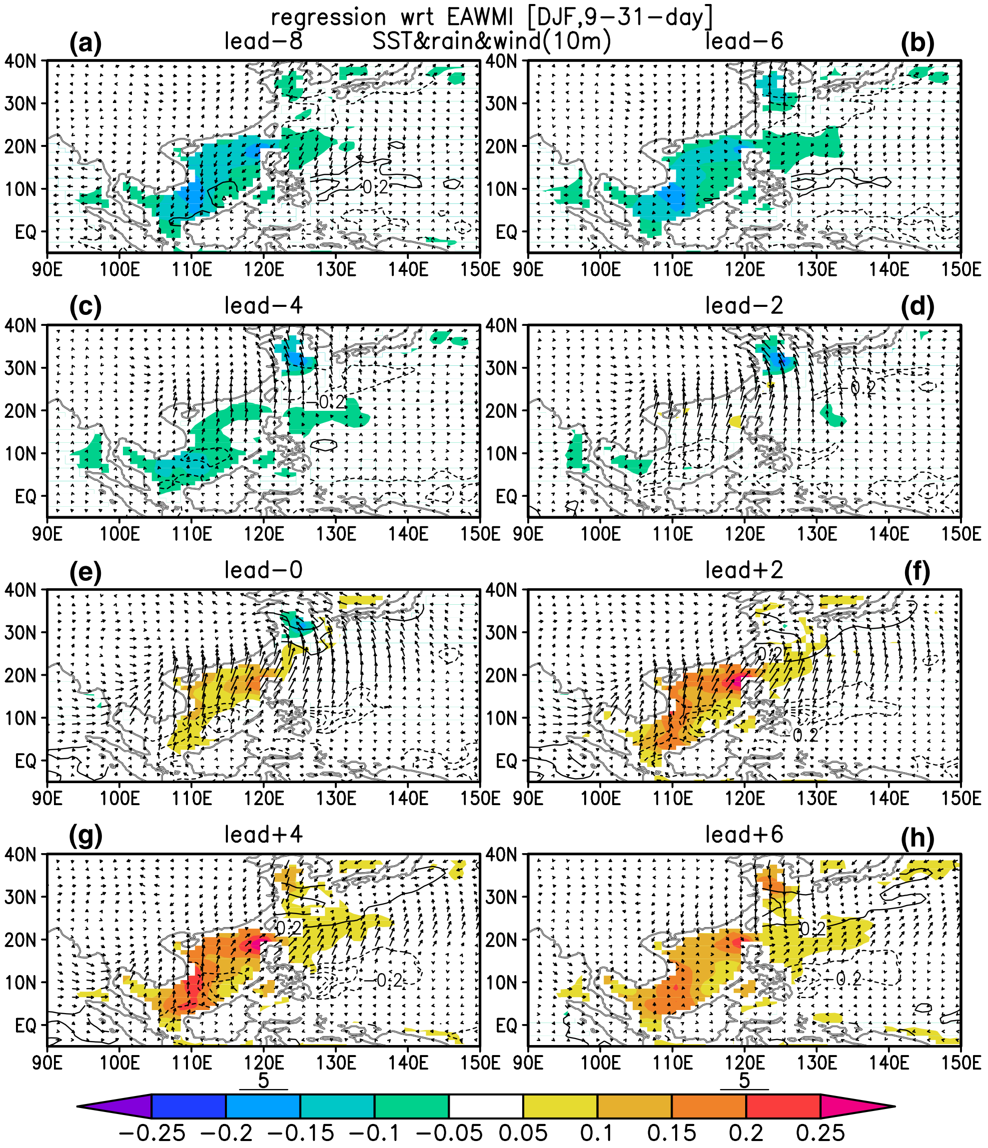

Fig. 6 Anomalies of SST (*shading*, unit: °C), rain rate (contour with zero contour suppressed, interval: 0.2 mm/day), and 10 m wind (vector with scale at bottom, unit: m/s) from 8 days before (lead −8) to 6 days after (lag +6) obtained by regression with respect to the normalized EAWMI for the period December 1 through February 28

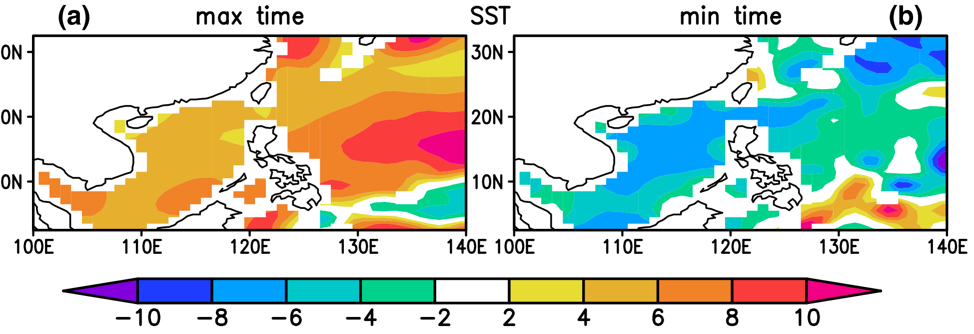

Fig. 7 Time (day) when the SST anomalies reach the maximum (**a**) and minimum (**b**) values with respect to the EAWMI for the period December 1 through February 28. Negative and positive time denotes before and after the peak EAWMI, respectively

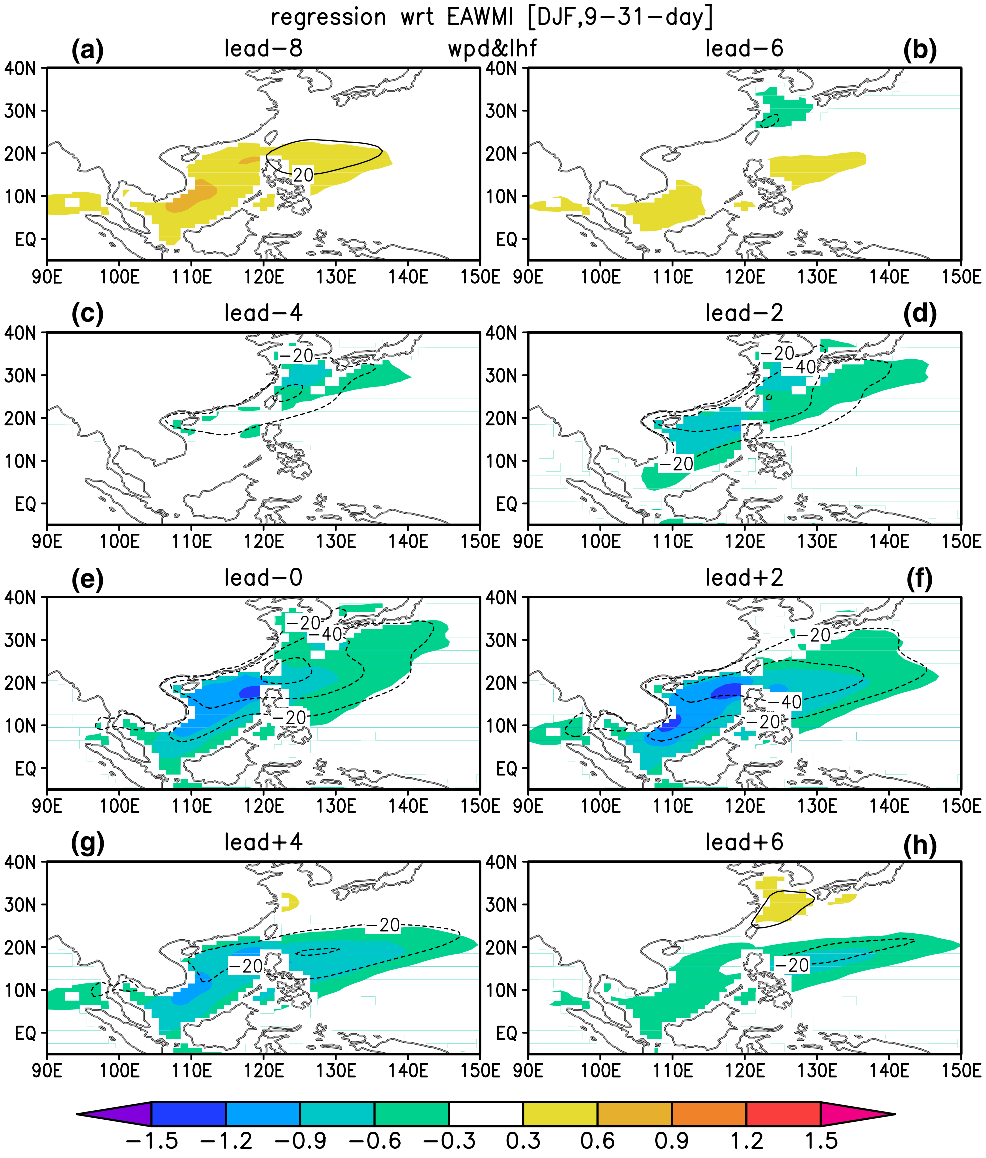

Fig. 8 Anomalies of surface wind speed (*shading*, unit: m/s) and surface latent heat flux (contour with zero contour suppressed, interval: 20 W/m^2) from 8 days before (lead −8) to 6 days after (lag +6) obtained by regression with respect to the normalized EAWMI for the period December 1 through February 28

The largest intraseasonal SST anomalies are observed in the SCS region (Fig. 6). The SST anomalies are particularly large to west of the Luzon Strait and in the region extending southward from central Vietnam coast, consistent with Wu and Chen (2015). Negative SST anomalies extend from the SCS northeastward to the western North Pacific at leads −8 and −6 (Fig. 6a, b). They weaken first in northern part at lead −4 (Fig. 6c) and then in southern part of the SCS at lead −2 (Fig. 6d). Positive SST anomalies appear and intensify first in northern part (Fig. 6e) and then in southern part of the SCS (Fig. 6f, g). Thus, the SST anomalies display a southward migration in the SCS region. Another region of negative SST anomalies is the Yellow Sea. In this region, SST anomalies are negative during leads −8 to −0 (Fig. 6a–e) and positive during leads +4 to +6 (Fig. 6g, h).

The SST anomalies display some localized features, which somewhat masks the southward propagation feature. To further demonstrate the southward propagation of SST anomalies, we extract the times when the SST anomalies reach maximum and minimum values at each grid point and plot these times in one map (Fig. 7). The time of positive SST anomalies displays a clear southward increase in the SCS and most of the tropical western North Pacific (Fig. 7a). The difference between northern and southern SCS is about 2 days. The time of negative SST anomalies shows a southward increase as well in most of the SCS and tropical western North Pacific except for coastal regions (Fig. 7b).

Opposite surface wind anomalies are seen between the SCS and mid-latitude East Asia at lead −8 (Fig. 6a). Correspondingly, anomalous divergence is expected over southern China and subtropical western North Pacific, accompanied by less rain. Southerly wind anomalies move southward to southern China at lead −6 (Fig. 6b), to the coast of southern China and northern SCS at leads −4 and −2 (Fig. 6c, d), and to the SCS at leads −0 to +4 (Fig. 6e–g). At the same time, anomalous divergence region moves southward and rain is reduced over southern SCS starting from lead −4. Anomalous convergence develops in the subtropical region starting from lead −4, accompanied by more rain after lead −2. Anomalous easterly winds appear over the Yellow Sea and the Japan Sea at leads −0 to +4 (Fig. 6e–g). After lead +2, the wind anomalies weaken in most regions (Fig. 6g, h). A north–south dipole pattern of rain anomalies is visible with more rain in subtropics and less rain in tropics starting from lead −0 (Fig. 6e–h).

The surface wind speed anomalies display an evolution consistent with the surface wind anomalies. As climatological winds are northeasterly in winter over the SCS and subtropical western North Pacific, southerly wind anomalies are accompanied by weaker surface wind speed. The surface wind speed is enhanced over the SCS at leads −8 and −6 (Fig. 8a, b) as anomalous winds are in the same direction as climatological winds. Over the subtropics, surface wind speed is reduced due to the opposite direction between anomalous and climatological winds. The positive wind speed anomalies in the south weaken and the negative wind speed anomalies in the north intensify and move southward in the following days (Fig. 8b–d). At leads 0 and +2, negative wind speed anomalies extend from the SCS northeastward to subtropical western North Pacific (Fig. 8e, f). At the subsequent days, wind speed anomalies weaken and move southward (Fig. 8g, h). At lead +6, wind speed is enhanced over the Yellow Sea and the East China Sea (Fig. 8h), following the appearance of northerly wind anomalies (Fig. 6h). The distribution and evolution of surface latent heat flux anomalies follow closely those of surface wind speed anomalies during the course. This suggests that the wind speed may be a dominant factor for surface evaporation change.

The cloud liquid water and surface net shortwave radiation changes are in tandem with the rain anomalies. A north–south contrast pattern of cloud liquid water and shortwave radiation anomalies is prominent between tropics and subtropics (Fig. 9). At 6–8 days before the peak EAWMI, a band of less liquid water and more shortwave radiation extends from southern China to Japan and a band of more liquid water and less shortwave radiation extends from southern SCS to the Philippine Sea (Fig. 9a, b). After the peak EAMI, the contrast pattern reverses its polarity, with less liquid water and more shortwave radiation in the south and more liquid water and less shortwave radiation in the north, respectively (Fig. 9e–h). This reversal appears to be accomplished in a few days (Fig. 9c, d). Thus, compared to surface wind speed and latent heat flux anomalies, the southward propagation appears not so obvious in cloud liquid water and shortwave radiation anomalies.

The southward move of surface wind and latent heat flux anomalies is obvious. The southward move of SST anomalies is also visible though not as obvious as surface wind and latent heat flux anomalies. The negative latent heat flux anomalies lead positive SST anomalies, indicative of an important contribution of surface heat flux to SST change. Negative SST anomalies in southern SCS lead negative rain anomalies, suggestive of an impact of SST on atmosphere. The SST impact may include both the thermal contrast between the SCS and the surrounding regions in association with the SST anomalies in the SCS and the regional SST anomaly gradient in the SCS region. For example, the presence of large SST anomalies in the SCS leads to a thermal contrast with the land to the north, which is favorable to the development of meridional wind anomalies over southern China and northern SCS (Fig. 6). Over southern SCS, large positive SST anomalies are located to west, whereas large negative rain anomalies appear over east in the SCS during lead −0 to +6 (Fig. 6e–h). This appears to support the role of the SST anomaly gradient in the formation of rain anomalies (Lindzen and Nigam 1987). These imply a coupled variation between SST and surface wind and surface heat flux, which will be elaborated in the next section.

5 Southward propagation of intraseasonal anomalies and their relationship

Analysis in the previous section shows a coherent southward propagation in SST, surface wind, and latent heat flux anomalies. To further understand the southward propagation of these anomalies and the relation between different variables, we display in Figs. 10, 11 Hovmöller diagrams of anomalies of different variables along 107.5°–120°E and 120°–135°E, respectively, on the 9–31-day time period. The former represents the South China Sea region and the latter the western North Pacific region.

Along 107.5°–120°E, the SST anomalies take about 2 days to move from the coast of South China to the equatorial region (Fig. 10a). Negative SST anomalies appear about 6–10 days before and positive SST anomalies occur about 2–6 days after the peak EAWMI. The wind anomalies display southward propagation from subtropics to equatorial SCS. Over the SCS, southerly (northerly) anomalies lead positive (negative) SST anomalies. The

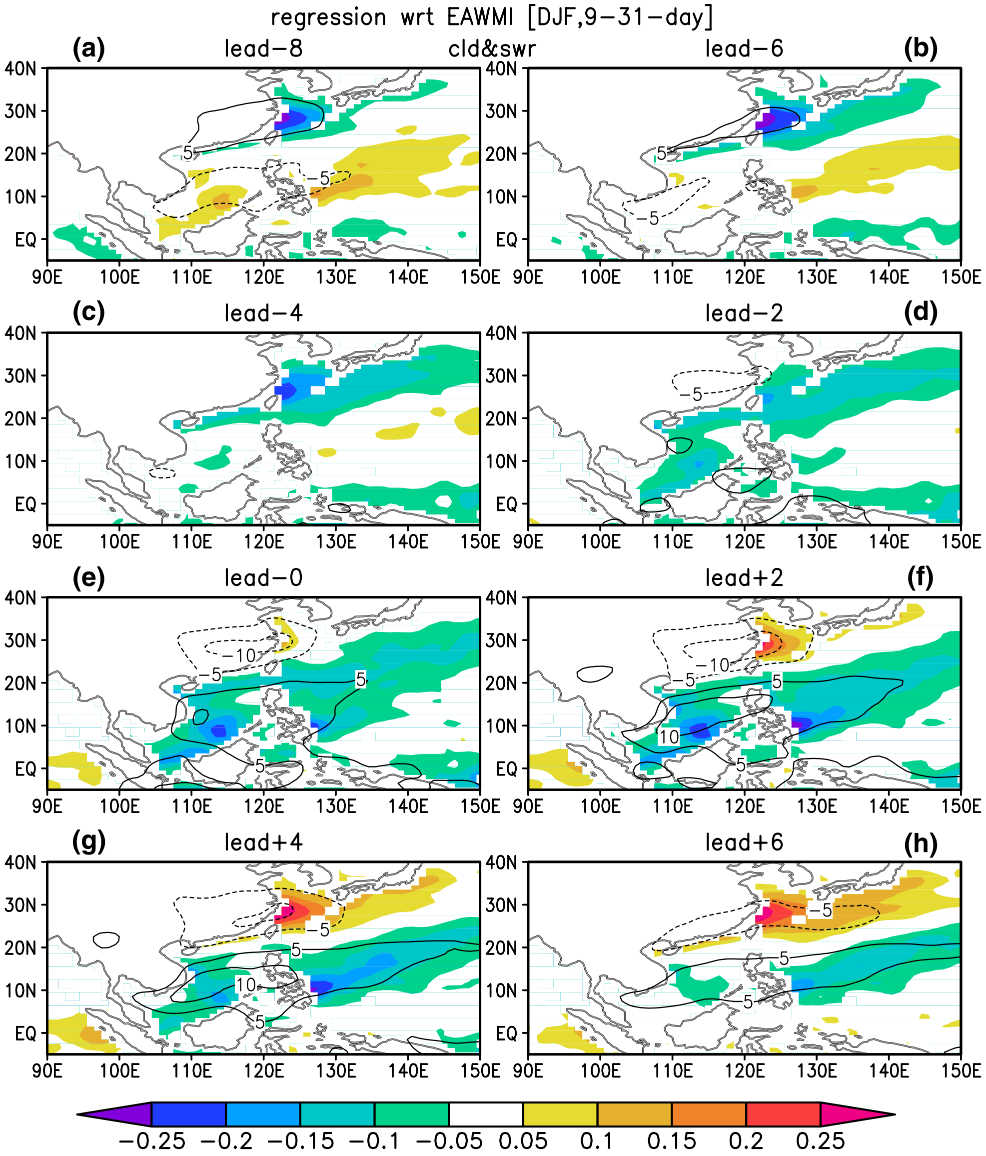

Fig. 9 Anomalies of cloud liquid water (*shading*, unit: mm) and surface net shortwave radiation (contour with zero contour suppressed, interval: 5 W/m^2) from 8 days before (lead −8) to 6 days after (lag +6) obtained by regression with respect to the normalized EAWMI for the period December 1 through February 28

surface wind speed anomalies display an obvious southward propagation with weaker wind speed leading higher SST by about 2 days (Fig. 10e). Southward propagation from southern China is obvious in latent heat flux anomalies as well (Fig. 10f). The latent heat flux anomalies tend to be in phase with wind speed anomalies. The latent heat flux anomalies are apparently larger in northern SCS than in southern SCS. This feature is likely due to the dependence of latent heat flux anomalies on climatological mean sea–air humidity difference, which is larger in northern SCS than in southern SCS (figure not shown).

The propagation feature is not clear in rain, cloud liquid water, and shortwave radiation anomalies. The rain anomalies show an opposite pattern north and south of approximately 15°N, with the magnitude larger in the tropics than in the subtropics (Fig. 10b). The GPCP rain anomalies display a northward extension to 30°–35°N (figure not shown). The reversal of rain anomalies occurs a few days earlier in southern SCS than in northern SCS. Compared to wind anomalies, less (more) rain occurs in regions of wind divergence (convergence) (Fig. 10a, b). The phase relation between rain and SST anomalies is very different in northern and southern SCS. In southern SCS, less rain leads positive SST anomalies, whereas in northern SCS rain and SST tend to vary in phase (Fig. 10a, b). This suggests a difference in the SST-rain

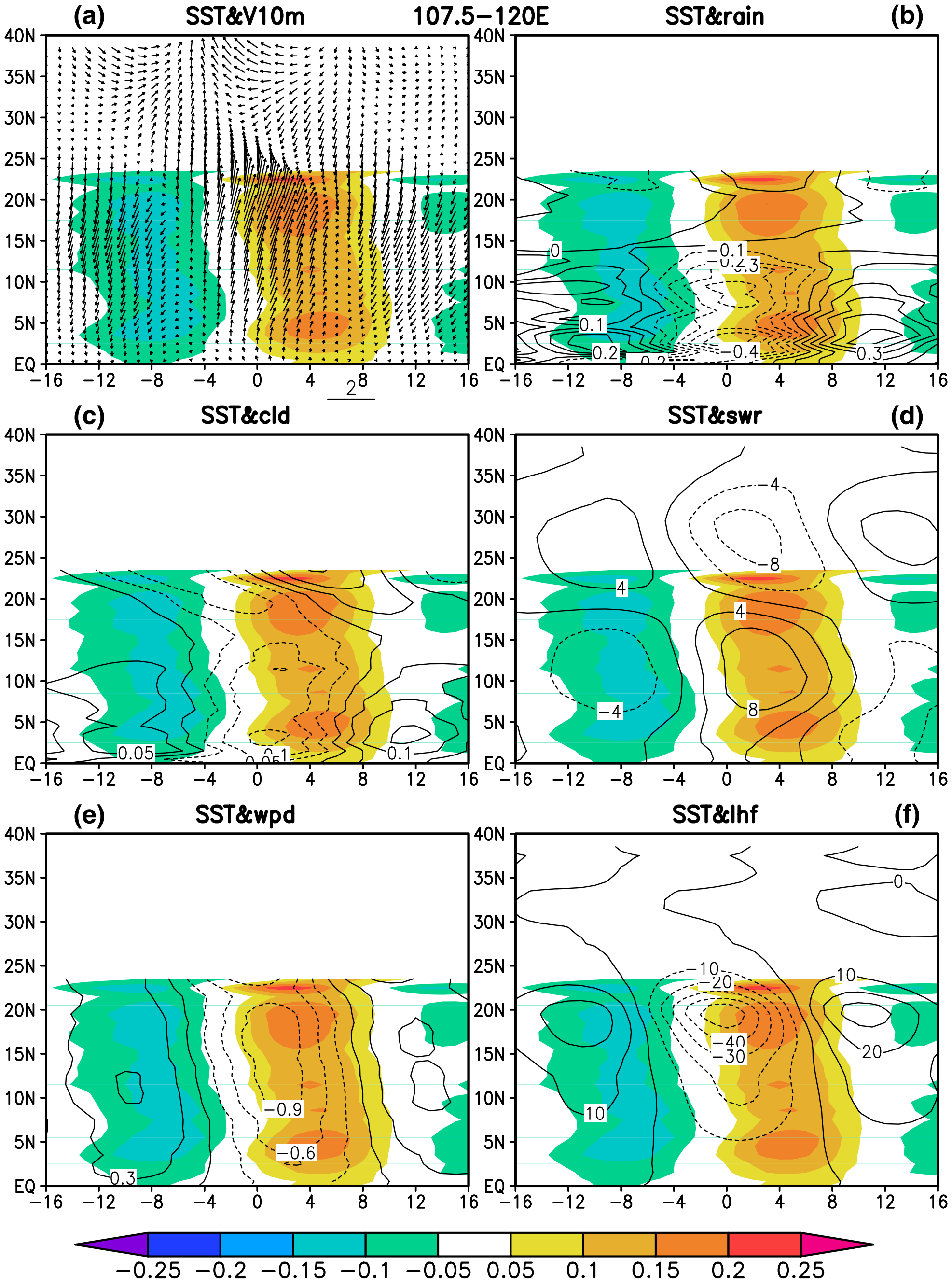

Fig. 10 Hovemöller diagrams of anomalies along 107.5°–120°E of SST (*shading*, unit: °C) and 10 m wind (m/s, scale at bottom) (**a**), rain rate (interval: 0.1 mm/day) (**b**), cloud liquid water (interval: 0.1 mm) (**c**), surface net shortwave radiation (interval: 4 W/m^2) (**d**), surface wind speed (interval: 0.3 m/s) (**e**), and surface latent heat flux (interval: 10 W/m^2) (**f**) from 16 days before to 16 days after the EAWMI obtained by regression with respect to the normalized EAWMI

relationship between northern and southern SCS. Such a difference was noted for monthly mean anomalies in winter (He and Wu 2013). Less cloud liquid water occurs before higher SST in the SCS, but with the time lead longer near the coast of South China (Fig. 10c). Shortwave radiation anomalies display opposite signs in subtropics and tropics (Fig. 10d). A reversal of shortwave radiation anomalies is observed about 4 days before peak EAWMI. The magnitude of shortwave radiation anomalies is much smaller than that of latent heat flux anomalies (Figs. 9f, 10d).

Overall, along the SCS longitude, SST, surface wind, and latent heat flux anomalies show coherent southward propagation, with weaker winds and less latent heat flux

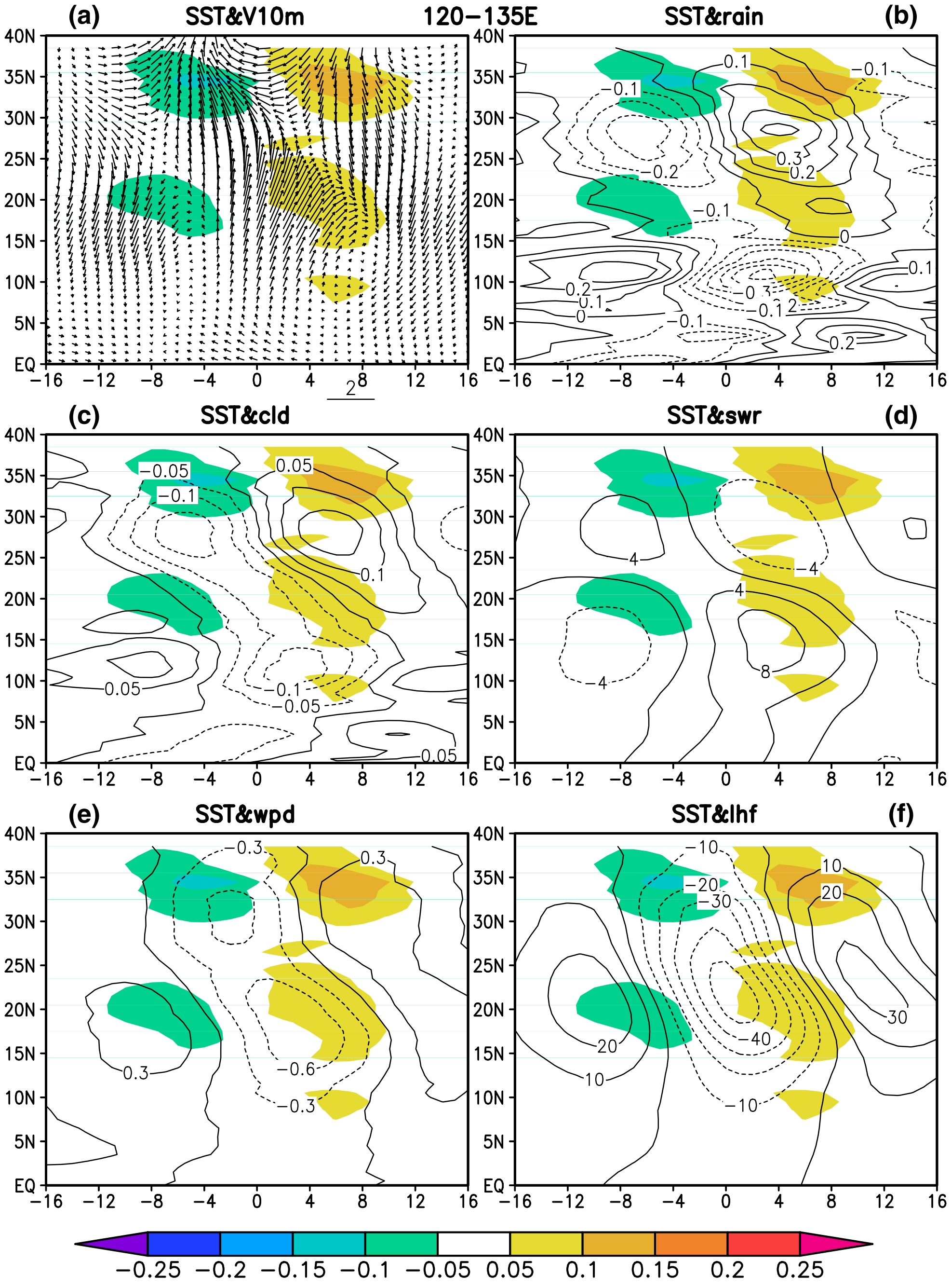

Fig. 11 The same as Fig. 10 except along 120°–135°E

leading higher SST. This indicates that the wind-evaporation effect is an important factor for the SST change. As the wind anomalies start over subtropics, it suggests that they may originate from the mid-latitude region. The rain, cloud, and shortwave radiation are dominated by stationary variations with opposite anomalies in tropics and subtropics. The shortwave radiation contributes to the SST change in the tropics, supplementary to the effect of latent heat flux.

Along 120°–135°E, SST anomalies are observed in two regions. One is the Yellow Sea and the other is to the east of the Luzon Strait (Fig. 11a). The latter one is an extension from the SCS. The magnitude of SST anomalies in the above regions is smaller compared to those in the SCS. This is likely because the mean mixed-layer depth is larger in subtropical western North Pacific than in the SCS (de Boyer Montégut et al. 2004). The SST anomalies show southward propagation in these regions, but with a

Fig. 12 Area-mean anomalies of SST (°C, *red line*), surface latent heat flux (W/m^2, *green-solid line*), surface wind speed (m/s, *green-dashed line*), surface net shortwave radiation (W/m^2, *blue-solid line*) and cloud liquid water (mm, *blue-dashed line*) averaged over the region of **a** 7.5°–17.5°N, 110°–120°E and **b** 27.5°–37.5°N, 120°–130°E from 16 days before to 16 days after the EAWMI obtained by regression with respect to the normalized EAWMI

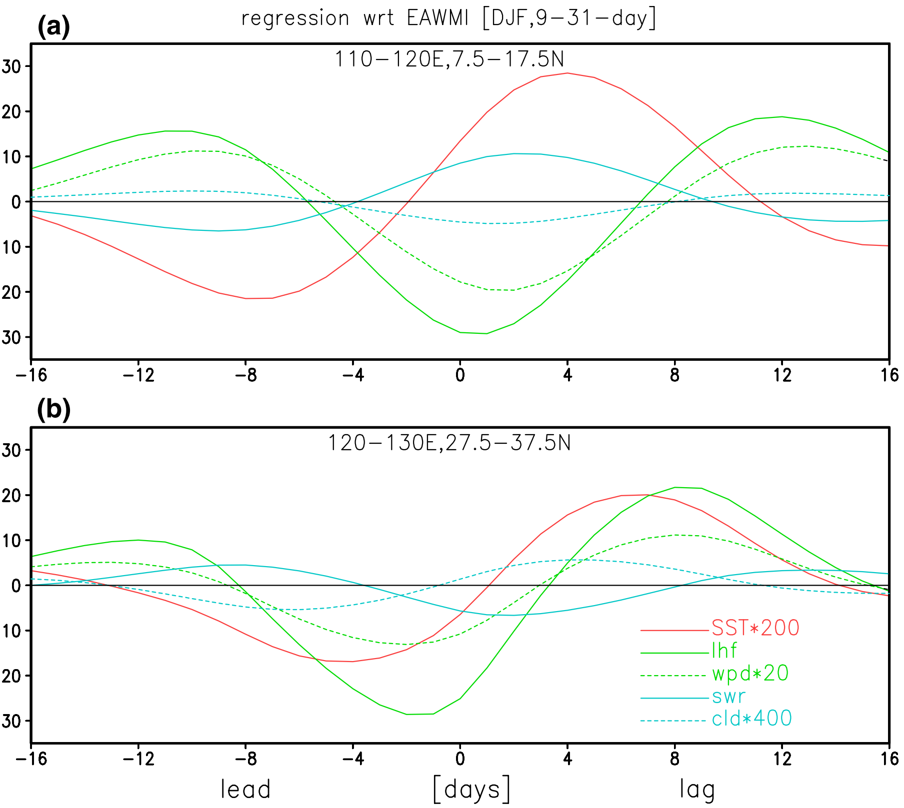

limited meridional extent. Surface wind anomalies display southward propagation from the mid-latitude to the tropics (Fig. 11a). Prominent southward propagation is observed in surface wind speed and latent heat flux anomalies as well (Fig. 11e, f). The latent heat flux anomalies are larger in subtropics. Negative latent heat flux anomalies are seen before higher SST in both subtropics and the mid-latitude, but with a longer time lead in the mid-latitude than in the subtropics.

The rain anomalies display a clear southward propagation from subtropics to tropics (Fig. 11b). The phase relation between rain and SST anomalies tend to be opposite in subtropics and the mid-latitude. In subtropics, negative rain anomalies lead positive SST anomalies, whereas in the mid-latitude, positive rain anomalies are observed before positive SST anomalies. The cloud liquid water anomalies display feature similar to the rain anomalies (Fig. 11c), so are shortwave radiation anomalies (Fig. 11d). The phase relation between SST and shortwave radiation anomalies indicates a contribution of shortwave radiation to the SST change in the subtropics, but not in the mid-latitude. In comparison, the magnitude of shortwave radiation anomalies is much smaller than that of latent heat flux anomalies (Figs. 10f, 11d).

Overall, along the western North Pacific longitude, SST anomalies are weaker and limited in the meridional propagation with two separate regions. The SST change is about 2 days later in the mid-latitude than in the subtropics. All the atmospheric variables and surface heat fluxes display southward propagation from the mid-latitude to the subtropics. Surface latent heat flux contributes to the SST change in both the subtropics and the mid-latitude. Shortwave radiation has a complementary contribution to the SST change in the subtropics, but has an opposite effect in the mid-latitude. The time lag between surface latent heat flux and SST is longer in the mid-latitude than in the subtropics.

To further compare the relation between SST and surface heat flux changes in the SCS and the Yellow Sea, we show in Fig. 12 area-mean anomalies averaged over the region of 7.5°–17.5°N, 110°–120°E and 27.5°–37.5°N, 120°–130°E. In the SCS, reduced latent heat flux and enhanced shortwave radiation both contribute to the SST warming (Fig. 12a). The latent heat flux change tends to follow the surface wind speed change and the shortwave radiation change is consistent with the cloud liquid water change. The magnitude of latent heat flux anomalies is about three times of that of shortwave radiation anomalies. Assuming a mixed layer depth of 30 m, a heat flux of 30 Wm^{-2} can induce an SST increase of 0.2 °C in about 10 days. This value is close to the magnitude of the SST tendency, indicative of an important contribution of surface heat flux to the SST change. In the Yellow Sea, latent heat flux is still an important factor for the weakening of negative SST

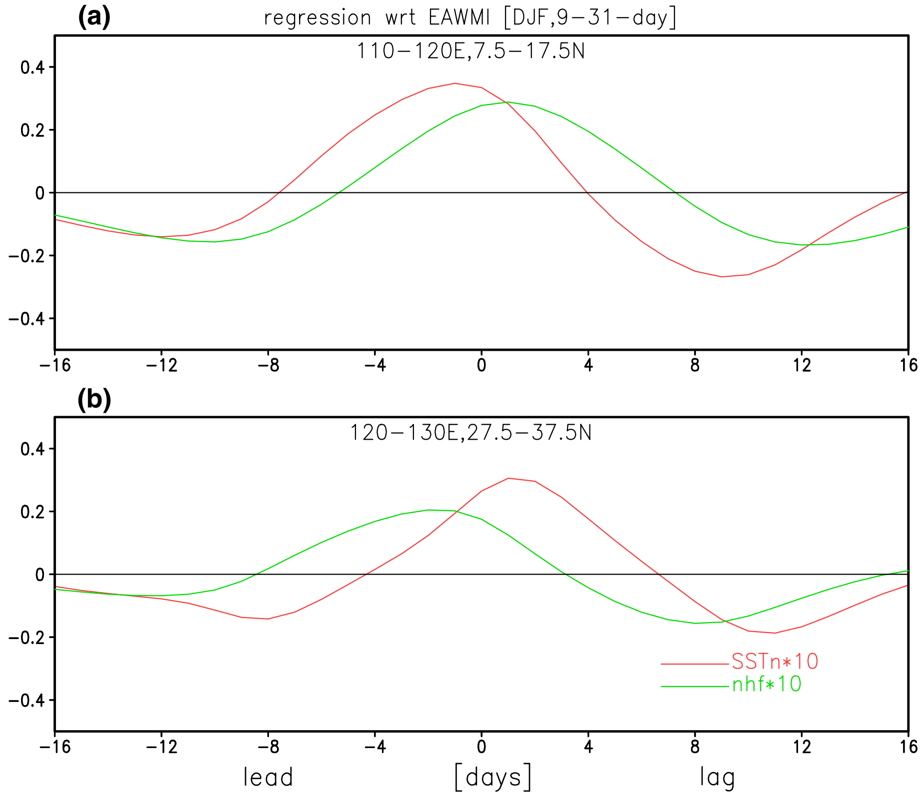

Fig. 13 Area-mean anomalies of SST tendency (°C/day, *red line*) and surface net heat flux converted to the SST tendency (°C/day, *green line*) averaged over the region of **a** 7.5°–17.5°N, 110°–120°E and **b** 27.5°–37.5°N, 120°–130°E from 16 days before to 16 days after the EAWMI obtained by regression with respect to the normalized EAWMI

anomalies (Fig. 12b). Shortwave radiation effect is negative, opposing the effect of latent heat flux from lead −4 to lead +4. Again, latent heat flux and shortwave radiation changes are consistent with surface wind speed and cloud changes, respectively. The surface heat flux cannot explain the increase of positive SST anomalies around lead +4. As such, other processes need to be considered to explain the SST warming. As seen from Fig. 11a, there are large easterly anomalies over the Yellow Sea during leads 0 to +8 days. The corresponding Ekman currents are expected to flow northward, transporting warmer ocean water from the subtropics. Climatologically, a large SST gradient is seen in the Yellow Sea (figure not shown). Hence, it is inferred that the wind-induced anomalous Ekman advection may contribute to the SST warming in the Yellow Sea.

For a quantitative demonstration of roles of surface heat flux in the SST change, we estimate the contribution of surface net heat flux (the sum of surface net shortwave radiation, surface net longwave radiation, surface latent and sensible heat fluxes) to the SST tendency. The SST tendency at a specific day is calculated as the difference of SST 1 day after minus SST 1 day before divided by 2 (days). The surface net heat flux anomalies are converted to the SST tendency assuming a constant mixed layer depth of 30 and 50 m for the SCS and Yellow Sea, respectively, based on de Boyer Montégut et al. (2004). Figure 13 compares the SST tendency and surface net heat flux anomalies in the SCS and Yellow Sea regions. In the SCS region, the surface net heat flux anomalies are of the same magnitude as the SST tendency (Fig. 13a), indicative of an important contribution of surface heat flux to the SST change. There is a phase shift between surface net heat flux and the SST tendency. This phase shift may suggest a contribution of oceanic processes. The discrepancy may also be contributed by inconsistency between SST and surface heat flux datasets of different sources. The surface heat flux contributes largely to the SST tendency in the Yellow Sea region from lead −4 to lag +2, but not from lag +3 to lag +6 (Fig. 13b). The phase shift between surface net heat flux and the SST tendency is larger compared to the SCS region. This may suggest a larger effect of oceanic processes on the SST change in the Yellow Sea region. Further analysis with reliable oceanic data with daily temporal resolution is needed to investigate the contribution of various oceanic processes to the SST change.

Distinguishing from boreal summer when northward propagation of intraseasonal signals dominates, southward propagation is prominent in boreal winter over the SCS and the western North Pacific. This difference may be interpreted based on climatological mean winds. In boreal winter, negative SST anomalies in the SCS induce lower-level divergence (Lindzen and Nigam 1987) with southerly anomalies over northern SCS (Figs. 6c, d, 10a). This reduces surface wind speed and upward latent heat flux

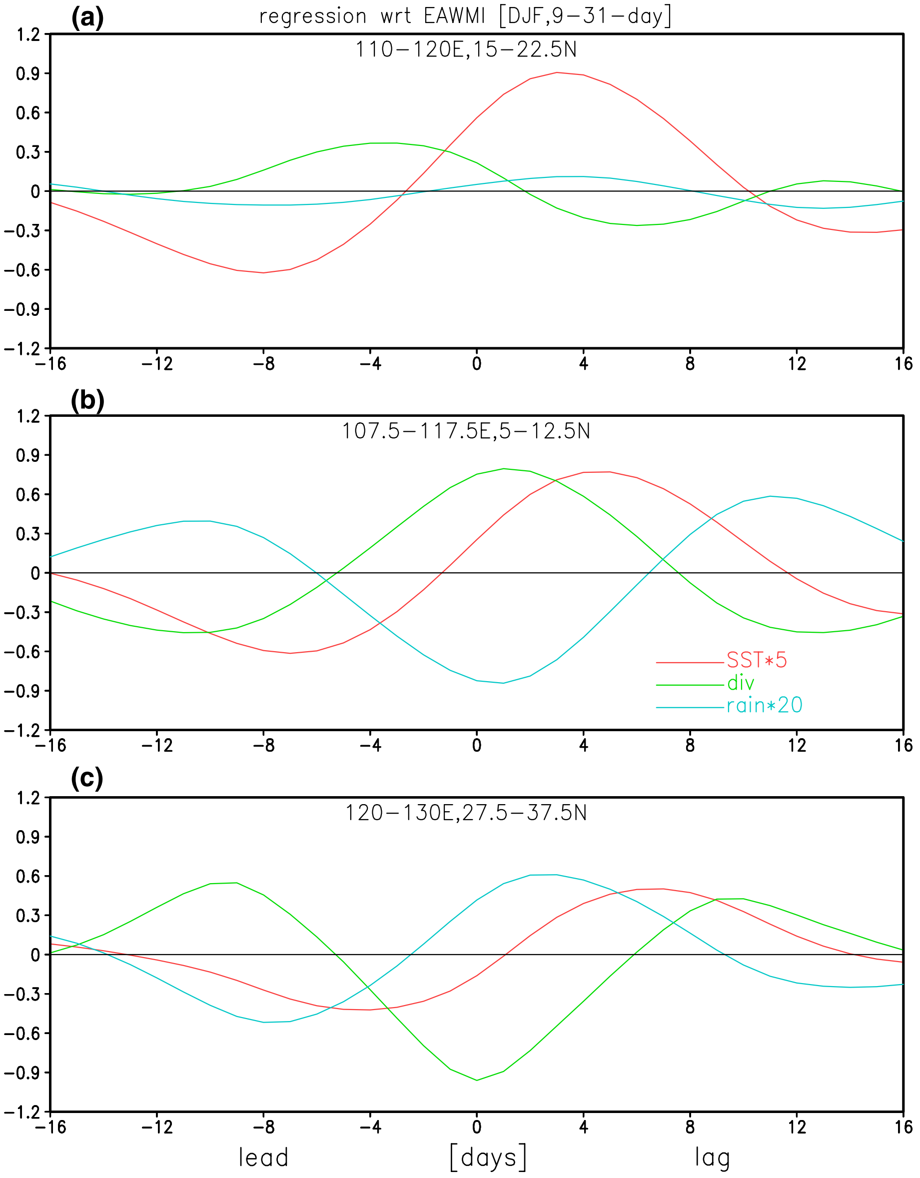

Fig. 14 Area-mean anomalies of SST (°C, *red line*), surface wind divergence (10^{-6} s^{-1}, *green line*), and rain rate (mm/day, *blue line*) averaged over the region of (**a**) 15°–22.5°N, 110°–122.5°E, **b** 5°–12.5°N, 107.5°–117.5°E, and **c** 27.5°–37.5°N, 120°–130°E from 16 days before to 16 days after the EAWMI obtained by regression with respect to the normalized EAWMI

over northern SCS (Figs. 8d, e, 10e–f). The decreased latent heat flux leads to a weakening of negative SST anomalies in northern SCS (Fig. 10a). As such, the region of negative SST anomalies shifts southward. In turn, the region of southerly wind anomalies with reduced latent heat flux displaces southward. Thus, the mechanism for southward propagation includes an impact of SST anomalies on lower-level winds and a feedback of wind-induced surface latent heat flux on SST. We note, however, that internal dynamics contributes to surface wind intensification, which will be discussed later.

To examine the SST impact on atmosphere, we compare in Fig. 14 the temporal evolution of SST, lower-level convergence, and rain anomalies in the SCS and the Yellow Sea regions. As the SST-rain relationship displays difference between northern and southern parts, we construct area-mean anomalies separately for northern and southern SCS. In the northern SCS region, negative (positive) SST anomalies tend to be followed by less (more) rain and anomalous lower-level divergence (convergence) (Fig. 14a). This suggests an impact of SST on atmosphere. The rain anomalies, however, are small. In the southern SCS region, positive SST anomalies are preceded by less rain rate and anomalous surface divergence, but followed by more rain rate and anomalous surface convergence (Fig. 14b). This appears to indicate a feedback of the SST anomalies on the atmosphere after they are induced by atmospheric changes. The area-mean anomalies, however, may not be able to show the impact of regional SST anomaly gradient in the SCS region. In contrast, in the Yellow Sea region, anomalous surface convergence and more rain occur before positive SST

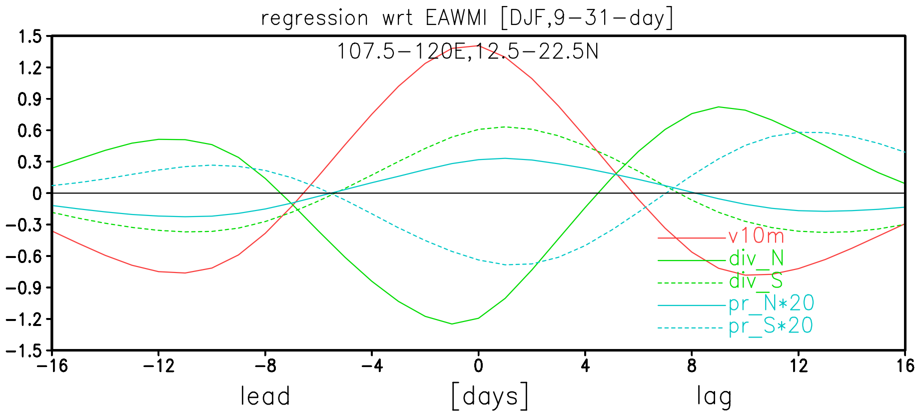

Fig. 15 Area-mean anomalies of 10 m meridional wind (m/s, *red line*) over the region of 12.5°–22.5°N, 107.5°–120°E, divergence (10^{-6} s^{-1}, *green-solid*) and rain rate (mm/day, *blue-solid*) over the region of 22.5°–32.5°N, 107.5°–120°E, divergence (10^{-6} s^{-1}, *blue-solid line*) and rain rate (10^{-6} s^{-1}, *blue-dashed line*) over the region of 2.5°–12.5°N, 107.5°–120°E from 16 days before to 16 days after the EAWMI obtained by regression with respect to the normalized EAWMI

anomalies (Fig. 14c). As such, local SST impact on the atmosphere is not clear. As noted above, the SST change appears as a response to the atmospheric wind changes through surface latent heat flux and Ekman advection in this region.

The southerly wind anomalies over northern SCS experience an obvious intensification during leads −4 to 0 days when the SST anomalies are small (Fig. 10a). This feature appears to be related to an interaction between circulation and precipitation. Accompanying southerly wind anomalies, anomalous surface divergence and convergence occur in south and north parts of southerly wind anomalies, respectively. This leads to a north–south contrast of rain anomalies. This further enhances southerly wind anomalies by a positive feedback. This is demonstrated in Fig. 15 that compares the temporal evolution of surface meridional wind anomalies in the SCS and divergence and rain anomalies to the north and south. An obvious intensification is seen in southerly wind anomalies over the SCS and surface divergence and rain anomalies to the north and south around lead −2 (Fig. 15) when the SCS SST anomalies are weak (Fig. 14a). As the lower boundary forcing is small, the amplification may be attributed to internal atmospheric processes.

6 Summary and discussions

Present analysis reveals prominent intraseasonal variations during boreal winter in both the SCS SST and EAWM. A spectrum peak is detected in the 9–31-day band for variations of both the SCS SST and EAWMI. The intraseasonal variations in the SCS SST and EAWM display obvious phase relationship. A weak (strong) EAWM leads warmer (cooler) SST and is preceded by cooler (warmer) SST in the SCS and subtropical western North Pacific.

The SST, surface wind, and latent heat flux anomalies displaycoherent southward propagation in the SCS longitude. The southward propagation is related to the wind-evaporation-SST effect under climatological northeasterly winds. Negative SST anomalies in the SCS and the related SST gradient induce southerly wind anomalies to the north, reducing surface wind speed and latent heat flux. In turn, the reduced surface latent heat flux weakens negative SST anomalies, first in northern SCS. This leads to a southward displacement of negative SST anomaly region along with reduced surface wind speed and latent heat flux region. Due to the effect of surface heat fluxes, SST anomalies change to positive, first in northern SCS. With the reversal of SST anomalies, surface wind anomalies turn to northerly, enhancing surface wind speed and latent heat flux, which, in turn, reducing positive SST anomalies in northern SCS. Consequently, this leads to the southward shift of positive SST anomalies.

The surface wind anomalies over southern China and northern SCS experience amplification during the period when the SST anomalies are weak. This intensification appears to be due to a positive feedback between circulation and precipitation. After meridional wind anomalies are initiated, a north–south dipole pattern of rain anomalies is induced due to a contrast of anomalous surface divergence. In turn, the rain anomaly pattern intensifies the meridional wind anomalies.

There are differences in the effect of surface heat flux in the SST change between the SCS and the Yellow Sea. In the SCS region, surface latent heat flux plays a dominant role in the intraseasonal variations of SST, with a complementary contribution from surface shortwave radiation. In the

Yellow Sea, surface latent heat flux is a main factor for the SST variation during the weakening period of SST anomalies. Surface shortwave radiation has a negative effect to the SST change. Wind-induced Ekman advection appears to be important for the SST change during the warming period after the peak EAWMI.

In boreal summer, active convection occurs frequently over the South China Sea and western North Pacific regions. The convective activity generates intraseasonal atmospheric variations that propagate northward or northwestward through different mechanisms (Hsu and Weng 2001; Chou and Hsueh 2010). Thus, northward propagation is a prominent feature of intraseasonal oscillations in boreal summer over the South China Sea and western North Pacific regions. In boreal winter, convective activity over northern Tropics becomes less frequent and its role in the generation of intraseasonal oscillations over the South China Sea and the western North Pacific is not as important as in boreal summer. Yet, the present study detected a distinct southward propagation of intraseasonal signals in wind and SST over the South China Sea and subtropical western North Pacific after they were initiated over subtropics. The mechanism for this southward propagation appears to be related to the wind-evaporation-SST effect under mean northerly winds. Further studies are needed to understand this mechanism and the roles of mean winds.

Acknowledgements Comments of three anonymous reviewers have helped the improvement of this paper. This study is supported by National Key Basic Research Program of China grant (2014CB953902) and National Natural Science Foundation of China grants (41475081, 41275081, and 41530425). The TMI data were obtained from http://www.remss.com/missions/tmi. The NCEP reanalysis 2 data were obtained from ftp://cdc.noaa.gov/. The GPCP precipitation data were obtained from https://climatedataguide.ucar.edu/climate-data/gpcp-daily-global-precipitation-climatology-project.

References

Adler RF, Huffman GJ, Chang A, Ferraro R, Xie P, Janowiak J, Rudolf B, Schneider U, Curtis S, Bolvin D, Gruber A, Susskind J, Arkin P, Nelkin E (2003) The version 2 global precipitation Climatology Project (GPCP) monthly precipitation analysis (1979-present). J Hydrometeor 4:1147–1167

Annamalai H, Slingo JM (2001) Active/break cycles: diagnosis of the intraseasonal variability of the Asian summer monsoon. Clim Dyn 18:85–102

Chen Z, Wu R, Chen W (2014) Distinguishing interannual variations of the northern and southern modes of the East Asian winter monsoon. J Clim 27:835–851

Chou C, Hsueh YC (2010) Mechanisms of northward-propagating intraseasonal oscillation-A comparison between the Indian Ocean and the western North Pacific. J Clim 23:6624–6640

de Boyer Montégut C, Madec G, Fischer AS, Lazar A, Iudicone A (2004) Mixed layer depth over the global ocean: an examination of profile data and a profile-based climatology. J Geophys Res 109:C12003. doi:10.1029/2004JC002378

Duvel JP, Vialard J (2007) Indo-Pacific sea surface temperature perturbations associated with intraseasonal oscillations of tropical convection. J Clim 20:3056–3082

Fu X, Wang B, Li T, McCreary JP (2003) Coupling between northward propagating, intraseasonal oscillations and sea-surface temperature in the Indian Ocean. J Atmos Sci 60:1733–1753

Gao RZ, Zhou FX (2002) Monsoonal characteristics revealed by intraseasonal variability of sea surface temperature (SST) in the South China Sea (SCS). Geophys Res Lett 29(8):1222. doi:10.1029/2001GL014225

He Z, Wu R (2013) Seasonality of interannual atmosphere-ocean interaction in the South China Sea. J Oceanogr 69:699–712

Hsu HH, Weng CH (2001) Northwestward propagation of the intraseasonal oscillation in the western North Pacific during the boreal summer: structure and mechanism. J Clim 14:3834–3850

Jiang X, Li T, Wang B (2004) Structures and mechanisms of the northward-propagating boreal summer intraseasonal oscillation. J Clim 17:1022–1039

Kajikawa Y, Yasunari T (2005) Interannual variability of the 10–25- and 30–60-day variation over the South China Sea during boreal summer. Geophys Res Lett 32:L04710. doi:10.1029/2004GL021836

Kanamitsu M, Ebisuzaki W, Woollen J, Yang SK, Hnilo JJ, Fiorino M, Potter GL (2002) NCEP–DOE AMIP-II Reanalysis (R-2). Bull Am Meteor Soc 83:1631–1643

Kemball-Cook S, Wang B (2001) Equatorial waves and air–sea interaction in the boreal summer intraseasonal oscillation. J Clim 14:2923–2942

Lawrence DM, Webster PJ (2002) The boreal summer intraseasonal oscillation: relationship between northward and eastward movement of convection. J Atmos Sci 59:1593–1606

Lindzen RS, Nigam S (1987) On the role of sea surface temperature gradients in forcing low level winds and convergence in the tropics. J Atmos Sci 44:2418–2436

Maloney ED, Sobel AH (2004) Surface fluxes and ocean coupling in the tropical intraseasonal oscillation. J Clim 17:4368–4386

Roxy M, Tanimoto Y (2007) Role of SST over the Indian Ocean in influencing the intraseasonal variability of the Indian summer monsoon. J Meteor Soc Jpn 85:349–358

Roxy M, Tanimoto Y (2011) Influence of sea surface temperature on the intraseasonal variability of the South China Sea summer monsoon. Clim Dyn 39:1209–1218

Roxy M, Tanimoto Y, Preethi B, Terray P, Krishnan R (2013) Intraseasonal SST-precipitation relationship and its spatial variability over the tropical summer monsoon region. Clim Dyn 41:45–61

Waliser DE, Lau KM, Kim JH (1999) The influence of coupled sea surface temperatures on the Madden–Julian oscillation: a model perturbation experiment. J Atmos Sci 56:333–358

Waliser DE, Murtugudde R, Lucas LE (2004) Indo-Pacific ocean response to atmospheric intraseasonal variability: 2. Boreal summer and the intraseasonal oscillation. J Geophys Res 109:C03030. doi:10.1029/2003JC002002

Wang B, Wu R (1997) Peculiar temporal structure of the South China Sea summer monsoon. Adv Atmos Sci 14:177–194

Wang B, Webster P, Kikuchi K, Yasunari T, Qi Y (2006) Boreal summer quasi-monthly oscillation in the global tropics. Clim Dyn 27:661–675

Wentz FJ, Gentemann C, Smith D, Chelton D (2000) Satellite measurements of sea surface temperature through clouds. Science 288:847–850

Wheeler M, Kiladis GN (1999) Convectively coupled equatorial waves: analysis of clouds and temperature in the wavenumber-frequency domain. J Atmos Sci 56:374–399

Woolnough SJ, Slingo JM, Hoskins BJ (2000) The relationship between convection and sea surface temperature on intraseasonal timescales. J Clim 13:2086–2104

Wu R (2010) Subseasonal variability during the South China Sea summer monsoon onset. Clim Dyn 34:629–642. doi:10.1007/s00382-009-0679-4

Wu R, Chen Z (2015) Intraseasonal SST variations in the South China Sea during boreal winter and impacts of the East Asian winter monsoon. J Geophys Res. doi:10.1002/2015JD023368

Wu R, Kirtman BP, Pegion K (2008) Local rainfall-SST relationship on subseasonal time scales in satellite observations and CFS. Geophys Res Lett 35:L22706. doi:10.1029/2008GL035883

Xie SP, Chang CH, Xie Q, Wang D (2007) Intraseasonal variability in the summer South China Sea: wind jet, cold filament, and recirculations. J Geophys Res 112:C10008. doi:10.1029/2007jc004238

Yasunari T (1979) Cloudiness fluctuations associated with the northern hemisphere summer monsoon. J Meteor Soc Jpn 57:227–242

Ye KH, Wu R (2015) Contrast of local air–sea relationship between 10–20-day and 30–60-day intraseasonal oscillations during May–September over the South China Sea and the western North Pacific. Clim Dyn 45(11–12):3441–3459. doi:10.1007/s00382-015-2549-6

Zeng LL, Wang DX (2009) Intraseasonal variability of latent-heat flux in the South China Sea. Theor Appl Meteor 97(1):53–64. doi:10.1007/s00704-009-0131-z

Zhang C (2005) Madden–Julian oscillation. Rev Geophys 43:RG2003. doi:10.1029/2004RG000158